

# First Measurement of Quasi-Elastic $\Lambda$ Baryon Production in $\bar{\nu}_\mu$ Interactions in the MicroBooNE Detector

MICROBOONE-NOTE-1121-PUB

The MicroBooNE Collaboration  
[microboone\\_info@fnal.gov](mailto:microboone_info@fnal.gov)

October 2021

## Abstract

We present the first measurement of the cross section of Cabibbo-suppressed  $\Lambda$  baryon production, using data collected with the MicroBooNE detector when exposed to Neutrinos from the Main Injector beam at the Fermi National Accelerator Laboratory. The data analyzed correspond to  $2.2 \times 10^{20}$  protons on target of neutrino mode running and  $4.9 \times 10^{20}$  protons on target of anti-neutrino mode running. An automated selection is combined with hand scanning, with the former identifying five candidate  $\Lambda$  production events when the signal was unblinded, consistent with the GENIE prediction of  $5.3 \pm 0.8$  events. Several scanners were employed, selecting between three and five events, compared with a prediction from a blinded Monte Carlo simulation study of  $3.7 \pm 1.0$  events. Restricting the phase space to only include  $\Lambda$ 's that decay above MicroBooNE's detection thresholds, we obtain a flux averaged cross section of  $2.0_{-1.6}^{+2.1} \times 10^{-40}$  cm<sup>2</sup> when statistical and systematic uncertainties are combined.

## 1 Motivation

This note describes the first measurement of the cross section for Cabibbo-suppressed (direct)  $\Lambda$ -baryon production in a restricted phase space using the MicroBooNE detector. The MicroBooNE detector [1] is a liquid argon time projection chamber (LArTPC) with several years of accumulated data using the neutrinos produced by the Main Injector (NuMI) beam [2] at the Fermi National Accelerator Laboratory. This enables studies of rare processes such as the direct production of  $\Lambda$  baryons in interactions between muon anti-neutrinos and argon in the detector:

$$\bar{\nu}_\mu + \text{Ar} \rightarrow \mu^+ + \Lambda + X, \quad (1)$$

where  $X$  denotes additional final state particles with no strangeness. This process is poorly constrained by existing measurements [3, 4, 5, 6, 7, 8] and is sensitive to the physics of the underlying neutrino interaction and nuclear effects, including nucleon form factors and axial masses, hyperon-nucleus potentials, and final state interactions [9, 10, 11]. Such a process constitutes a potential source of background in proton decay experiments, such as DUNE [13, 12] and Hyper-Kamiokande [14]. If the  $\Lambda$  baryon undergoes a secondary interaction with a nucleon, a kaon can be produced, mimicking the  $p \rightarrow K + \nu$  signal in these experiments. Additionally, this process is exclusively the result of anti-neutrino interactions and therefore could be used to constrain contamination from anti-neutrinos in a neutrino beam.

This note describes the measurement of a restricted phase space cross section for direct  $\Lambda$  production using the MicroBooNE detector. To maximize data statistics, we combine data collected when the NuMI beam was operating in its neutrino (forward horn current, FHC) and anti-neutrino (reverse horn current, RHC) modes.

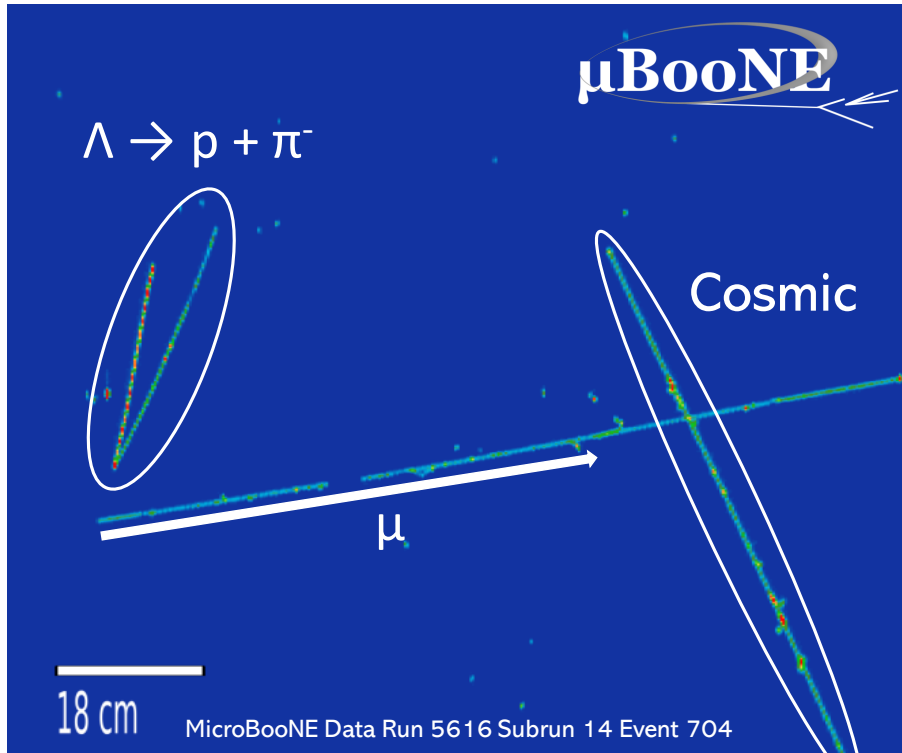


Figure 1: A candidate  $\bar{\nu}_\mu + \text{Ar} \rightarrow \mu^+ + \Lambda$  interaction observed in MicroBooNE data. A cosmic ray is also reconstructed in the event. The specific ionization is displayed by the color scale. There is a dead region without active wires around the centre of the muon track.

## 2 Event Selection

The selection searches for muon-anti-neutrino interactions with argon nuclei, in which a  $\Lambda$  is produced through the strangeness-violating quasi-elastic process and subsequently decays to a proton and negatively charged pion. This decay produces a distinctive V shaped signature in the detector, an example of which can be seen in Fig. 1.

We employ the GENIE [16] event generator to simulate neutrino interactions inside the MicroBooNE cryostat and surrounding material, in conjunction with GEANT 4 [17] for particle propagation and secondary interactions, followed by a simulation of the detector response to the interactions of those particles. The event selection employs the Pandora multi-algorithm reconstruction framework [18] which identifies a reconstructed neutrino vertex and the associated particles, which are classified as either tracks or showers.

To isolate  $\Lambda$  production events, we apply a number of criteria: a neutrino vertex must be reconstructed in the fiducial volume defined in an earlier analysis [15] with at least three associated tracks and no showers. Particle identification (PID) scores [19] are calculated for each track indicating whether they are muon-like or proton-like, and the longest muon-like track is selected as the muon candidate. An array of boosted decision trees [20] is employed to generate a response score from several variables such as PID scores and the Pandora track/shower classification score [21] to select a pair of tracks consistent with the  $\Lambda \rightarrow p + \pi^-$  decay. The reconstructed invariant mass  $W$  and angular deviation, defined as the angle between the line connecting the primary vertex to the decay vertex and the momentum vector of the  $\Lambda$  candidate, are calculated. Events with  $1.09 < W < 1.19$  GeV and angular deviation  $< 14^\circ$  are retained.

After deconvolution and noise removal [22, 23], the wire activity in the detector can be used to visualize the trajectories of particles produced in the interaction. This is the information displayed in Fig. 1, in which the green/red regions indicate nonzero activity in that wire plane. This is

analyzed to determine if the muon candidate and  $\Lambda$  candidate form separate “islands” of activity. This tests whether the  $\Lambda$  candidate created a true secondary vertex, a feature which discriminates  $\Lambda$  production from background processes with similar kinematics. This test is performed separately using information from each of the three wire planes, enabling identification of the decay vertex even when the orientation of the event makes this difficult when viewed from one of the planes. The island finding algorithm is described in detail in appendix D.

A visual scan of event displays of the selected data is performed to remove background selected due to reconstruction problems. To evaluate the background rejection power and reliability of this technique, a blinded study with five scanners was completed, using Monte Carlo (MC) simulated events that had passed the automated selection, with the results used to modify simulation predictions. To maintain blindness in the final measurement, a separate set of MC simulated events are mixed with the data from the signal region to conceal the number of data events from the scanners.

As an additional test to confirm the validity of the visual scanning procedure, an alternative analysis was performed without performing hand scanning. To constrain the predicted background due to reconstruction problems, a sideband is employed, created by inverting the cuts applied to the invariant mass and angular deviation. The result of this alternative selection and constraint are also used to calculate the cross section and yield a result consistent with the one obtained when performing the visual scan, albeit with slightly poorer sensitivity. This constraint method is described in appendix F.

After the event selection is complete, the background primarily consists of other sources of  $\Lambda$  baryons and hyperons, including other quasi-elastic-like interactions (“direct”), deep inelastic scattering (DIS) and resonant interactions (RES). A small number of background events produced by secondary interactions of neutrons is predicted, in which charged particles are liberated, most commonly  $p\pi^\pm$  and  $pp$  pairs, which can lead to a similar V shape. The remainder is due to mis-reconstruction of events. Cosmic ray and out-of-cryostat neutrino interactions (“dirt”) are included in the simulation but none pass the selection. The number of events from each category selected in the MC simulation are shown in Table 1.

Event Category	Selected MC	After Hand Scan
Signal	$2.5 \pm 0.1$	$2.3 \pm 0.4$
Other $\Lambda$	$0.7 \pm 0.2$	$0.5 \pm 0.3$
Other hyperons	$1.0 \pm 0.2$	$0.7 \pm 0.3$
Neutrons	$0.3 \pm 0.1$	$0.1 \pm 0.1$
Other	$0.9 \pm 0.3$	$0.1 \pm 0.1$
Total Background	$2.8 \pm 0.6$	$1.4 \pm 0.7$

Table 1: Events selected from Monte Carlo (MC) simulation using standard GENIE model parameters, before and after the hand scanning selection efficiencies are applied. Combined MC simulation statistical and systematic uncertainties are shown.

### 3 Systematic Uncertainties

Two sources of flux uncertainties are considered: the hadron production modelling and the beam-line geometry. The overall flux uncertainty in the predicted signal is small (approximately 10%), due to the high neutrino energy threshold for  $\Lambda$  production. The uncertainties on the production rate for the hadrons that subsequently decay into beam neutrinos dominate the flux uncertainty in this energy region [24].

To determine the uncertainties from the models used to derive the cross sections for background neutrino interactions, we use the results of the fits described in Ref. [25], with 44 parameters varied in parallel to produce 600 variations. In addition, we use predictions from 8 alternative models to estimate uncertainties resulting from parameters that are difficult to vary continuously.

Secondary interactions in the argon outside the nuclear remnant are described by GEANT 4 [17]; we use the Geant4Reweight [26] package to determine the uncertainties from the description of these reinteractions by varying proton, charged pion, and  $\Lambda$  baryon interaction cross sections. We assume an uncertainty of 20% on the proton and  $\Lambda$  interaction cross sections, while for the charged pions a pair of multi-target, multi-channel fits are performed using external data to extract uncertainties on the cross sections of individual interaction channels, as described in Ref. [26]. To include uncertainties on the neutron interaction cross sections, a fit is performed to data from the CAPTAIN experiment [27], yielding an uncertainty of 26% on the total  $n$ -Ar cross section. This uncertainty is included by re-scaling the rate of selected events containing secondary interactions of neutrons by  $\pm 26\%$ .

The uncertainties on the modeling of the detector response are estimated by simulating a set of neutrino interactions in the MicroBooNE detector, which are then fed into several detector models. These sets of events are reconstructed and then processed through the selection. The difference between the number of events selected using the standard detector model and an alternative model is used as an uncertainty. Four categories of detector uncertainties are considered: modeling of the quantity of scintillation light produced, the wire response [28], the space charge effect [29], and the recombination of argon ions.

The selection efficiencies and background acceptance rates of the five individual scanners are treated as five sets of predictions, the spread of which is used as an uncertainty.

## 4 Cross Section Extraction Procedure

The restricted phase space cross section,  $\sigma_*$ , is related to the number of events observed in data,  $N_{\text{obs}}$ , by:

$$\sigma_* = \frac{N_{\text{obs}} - B}{T\Phi\Gamma\epsilon}, \quad (2)$$

where  $B$  is the predicted number of background events,  $T$  the number of argon nuclei in the fiducial volume,  $\Phi$  the total muon anti-neutrino flux,  $\Gamma = 0.64$  the branching fraction for the process  $\Lambda \rightarrow p + \pi^-$  [30], and  $\epsilon$  the average selection efficiency. The relation between the restricted phase space cross section and the total cross section depends on the momentum distribution of the  $\Lambda$ 's produced, and is described in appendix B.

To account for the asymmetry in the data and MC simulation statistical uncertainties, we employ a Bayesian procedure to calculate the full posterior distribution on the extracted cross section. Bayesian posterior distributions of the selection efficiency and background acceptance are estimated with the TEfficiency class [31], while the distribution of the true data event rate is obtained through application of Bayes' theorem to the Poisson distribution. We use uniform priors for all three distributions.

Systematic uncertainties are included by calculating the fractional covariance between the selection efficiency, the  $\bar{\nu}_\mu$  flux, and the selected background:

$$\text{Frac. Cov.} = \begin{bmatrix} 0.0066 & 0.0185 & 0.2070 \\ -0.0012 & 0.0530 & 0.0185 \\ 0.0057 & -0.0012 & 0.0066 \end{bmatrix}. \quad (3)$$

Systematic uncertainties are then propagated through the cross section calculation by throwing systematic deviations,  $\alpha_\epsilon$ ,  $\alpha_\Phi$ , and  $\alpha_B$  using a three dimensional Gaussian distribution parameterised by their covariance matrix.

Values of the true data event rate  $N$ , the selected background and the efficiency are repeatedly thrown from their respective distributions alongside systematic deviations in efficiency, flux and background, and the cross section is calculated each time with:

$$\sigma_* = \frac{N - (B + \alpha_B)}{T(\Phi + \alpha_\Phi)\Gamma(\epsilon + \alpha_\epsilon)}, \quad (4)$$

where  $\alpha_B$ ,  $\alpha_\Phi$ , and  $\alpha_\epsilon$  are the systematic deviations. The resulting values are recorded in a histogram giving the Bayesian posterior probability distribution on the cross section.

## 5 Results and Outlook

After unblinding the signal region, 5 data events are selected by the automated selection. The invariant masses of the selected data events are compared with MC simulation predictions in Fig. 2. The five hand scanners selected 3, 3, 4, 4, and 5 data events from this sample. To extract the final cross section posterior distribution, we sum the Bayesian posterior distributions corresponding to observing those numbers of events and normalize the result to 1; the resulting distribution is shown in Fig. 3. We obtain a cross section of  $2.0^{+2.1}_{-1.6} \times 10^{-40}$  cm<sup>2</sup> (combining statistical and systematic uncertainties), a value consistent with predictions from the GENIE [16] and NuWro [9] event generators.

In summary, the first measurement of the rare channel of quasi-elastic-like  $\Lambda$  production in muon-anti-neutrino interactions with argon has been performed, employing novel methods to identify the  $\Lambda$  baryon decay vertex. As this is a rare channel, the dominant source of uncertainty is due to data statistics. Improvements in sensitivity can be achieved with better reconstruction and selection efficiencies, and with analyzing more data. Data collected between 2017 and 2020 awaits analysis, with which an approximately fourfold increase in events is expected.

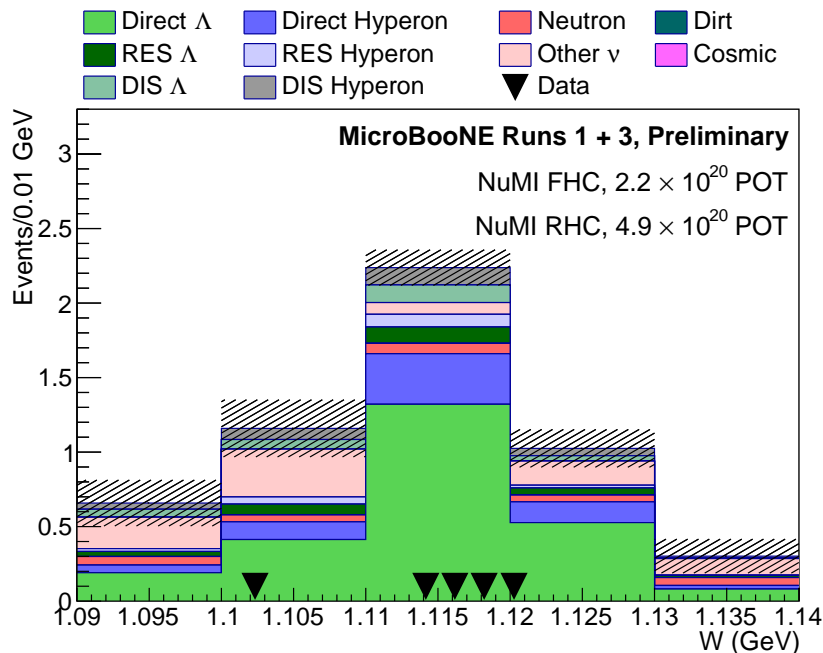


Figure 2: Selected MC simulation events and data shown as a function of the reconstructed invariant mass, when using the purely automated selection. Black triangles indicate the location of the selected data events. The mass of the  $\Lambda$  baryon is 1.115 GeV [30]. The hatched regions indicate combined statistical and systematic uncertainties.

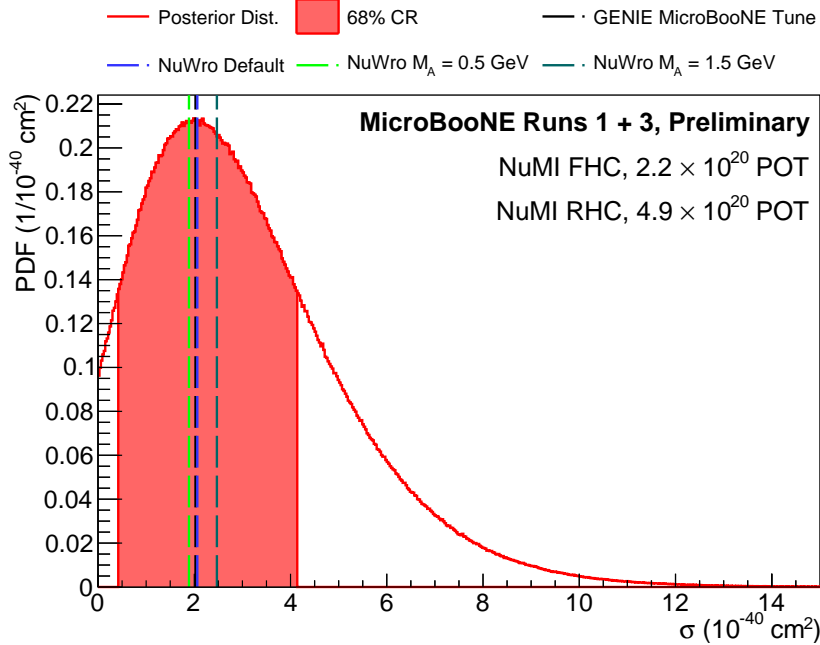


Figure 3: Posterior distribution describing the extracted cross section compared with the MicroBooNE GENIE tune [25] and several predictions from the NuWro event generator. The NuWro predictions include the effect of final state interactions, while GENIE does not take them into account. The standard axial mass used by NuWro is 1.03 GeV.

## References

- [1] R. Acciarri *et al.* (MicroBooNE), Design and construction of the MicroBooNE detector, *J. Instrum.* **12**, no.02, P02017 (2017)
- [2] L. Aliaga *et al.* (MINERvA), Neutrino Flux Predictions for the NuMI Beam, *Phys. Rev. D* **94**, no.9, 092005 (2016)
- [3] V. V. Ammosov *et al.*, Neutral Strange Particle Exclusive Production in Charged Current High-energy Anti-neutrino Interactions, *Z. Phys. C* **36**, 377 (1987)
- [4] T. Eichten *et al.*, Observation of 'Elastic' Hyperon Production by Anti-neutrinos, *Phys. Lett.* **40B**, 593 (1972)
- [5] O. Erriquez *et al.*, Production of Strange Particles in anti-neutrino Interactions at the CERN PS, *Nucl. Phys. B* **140** 123 (1978)
- [6] O. Erriquez *et al.*, Strange particle production by antineutrinos, *Phys. Lett. B* **70** 383 (1977)
- [7] J. Brunner *et al.* (SKAT), Quasielastic Nucleon and Hyperon Production by Neutrinos and Anti-neutrinos With Energies Below 30-GeV, *Z. Phys. C* **45** 551 (1990)
- [8] G. Fanourakis *et al.*, Study of low-energy antineutrino interactions on protons, *Phys. Rev. D* **21**, 562 (1980)
- [9] C. Thorpe *et al.*, Second class currents, axial mass, and nuclear effects in hyperon production, *Phys. Rev. C* **104**, no.3, 035502 (2021)
- [10] J. E. Sobczyk, N. Rocco, A. Lovato and J. Nieves, Weak Production of Strange and Charmed Ground-State Baryons in Nuclei, *Phys. Rev. C* **99**, no.6, 065503 (2019)

- [11] S. K. Singh and M. J. Vicente Vacas, Weak quasi-elastic production of hyperons, *Phys. Rev. D* **74**, 053009 (2006)
- [12] B. Abi *et al.* (DUNE), Deep Underground Neutrino Experiment (DUNE), Far Detector Technical Design Report, Volume II: DUNE Physics, arXiv:2002.03005 [hep-ex]
- [13] B. Abi *et al.* (DUNE), Prospects for beyond the Standard Model physics searches at the Deep Underground Neutrino Experiment, *Eur. Phys. J. C* **81**, no.4, 322 (2021)
- [14] K. Abe *et al.* (Hyper-Kamiokande), Hyper-Kamiokande Design Report, arXiv:1805.04163 [physics.ins-det]
- [15] P. Abratenko *et al.* (MicroBooNE), Cosmic Ray Background Rejection with Wire-Cell LArTPC Event Reconstruction in the MicroBooNE Detector, *Phys. Rev. Applied* **15**, no.6, 064071 (2021)
- [16] C. Andreopoulos *et al.*, The GENIE Neutrino Monte Carlo Generator, *Nucl. Instrum. Methods Phys. Res., Sect A* **614** 87 (2010)
- [17] S. Agostinelli *et al.* (GEANT4), GEANT 4—a simulation toolkit, *Nucl. Instrum. Meth. A* **506**, 250-303 (2003)
- [18] J. S. Marshall *et al.*, (MicroBooNE) The Pandora multi-algorithm approach to automated pattern recognition in LAr TPC detectors, *J. Phys. Conf. Ser.* **888**, no.1, 012142 (2017)
- [19] P. Abratenko *et al.* (MicroBooNE), Calorimetric classification of track-like signatures in liquid argon TPCs using MicroBooNE data, *J. High Energy Physics* **12**, 153 (2021)
- [20] A. Hoecker, *et al.* TMVA - Toolkit for Multivariate Data Analysis, arXiv:physics/0703039 [physics.data-an]
- [21] W. Van De Pontseele, Ph.D. thesis, Search for Electron Neutrino Anomalies with the MicroBooNE Detector, Oxford U, (2020), FERMILAB-THESIS-2020-11
- [22] C. Adams *et al.* (MicroBooNE), Ionization electron signal processing in single phase LArTPCs. Part I. Algorithm Description and quantitative evaluation with MicroBooNE simulation, *J. Instrum.* **13**, no.07, P07006 (2018)
- [23] C. Adams *et al.* (MicroBooNE), Ionization electron signal processing in single phase LArTPCs. Part I. Algorithm Description and quantitative evaluation with MicroBooNE simulation, *J. Instrum.* **13**, no.07, P07007 (2018)
- [24] L. Aliaga Soplín, Ph.D. thesis, Neutrino Flux Prediction for the NuMI Beamline, College of William and Mary (2016), FERMILAB-THESIS-2016-03
- [25] P. Abratenko *et al.* (MicroBooNE), New CC0 $\pi$  GENIE Model Tune for MicroBooNE, *Phys. Rev. D* **105**, no.7, 072001 (2022)
- [26] J. Calcutt, *et al.* Geant4Reweight: a framework for evaluating and propagating hadronic interaction uncertainties in Geant4, *J. Instrum.* **16**, no.08, P08042 (2021)
- [27] B. Bhandari *et al.* (CAPTAIN), First Measurement of the Total Neutron Cross Section on Argon Between 100 and 800 MeV, *Phys. Rev. Lett.* **123**, no.4, 042502 (2019)
- [28] P. Abratenko *et al.* (MicroBooNE), Novel approach for evaluating detector-related uncertainties in a LArTPC using MicroBooNE data, *Eur. Phys. J. C* **82**, no.5, 454 (2022)
- [29] P. Abratenko *et al.* (MicroBooNE), Measurement of Space Charge Effects in the MicroBooNE LArTPC Using Cosmic Muons, *J. Instrum.* **15**, no.12, P12037 (2020)

[30] P. A. Zyla *et al.* (Particle Data Group), Review of Particle Physics, Prog. Theor. Exp. Phys. **2020**, no.8, 083C01 (2020)

[31] <https://root.cern.ch/doc/master/classTEfficiency.html>, accessed May 2022. Root version 6.16 used.

# Appendices

## A Kinematic Variables

After identifying a pair of tracks to form the candidate  $\Lambda \rightarrow p + \pi^-$  decay, two kinematic variables are calculated: the invariant mass of the  $\Lambda$  candidate and the angular deviation. The distributions of these variables at this stage of the selection are displayed in Fig. 4. The calculation of the angular deviation is illustrated in Fig. 5.

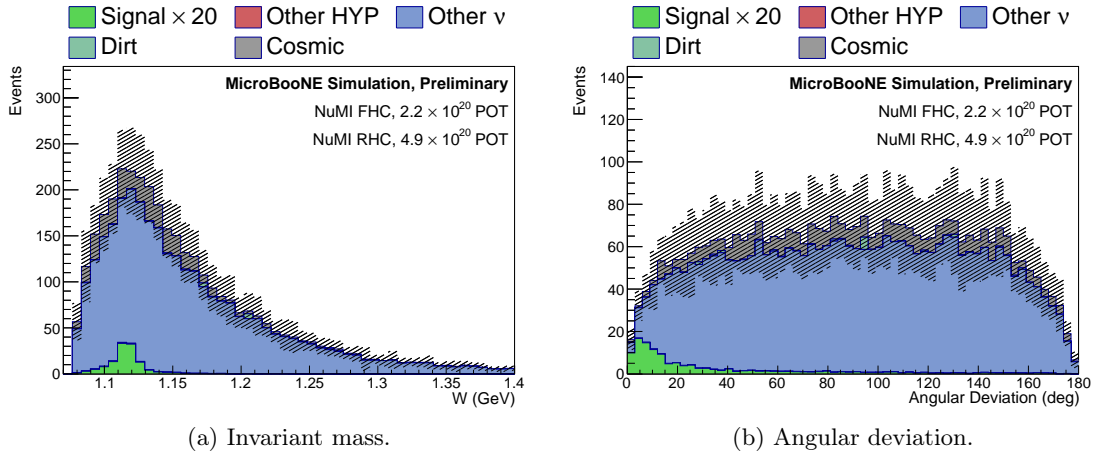


Figure 4: The kinematic variables employed by the event selection. The signal has been multiplied by 20 for visibility. The hatched regions indicate combined systematic and statistical uncertainties.

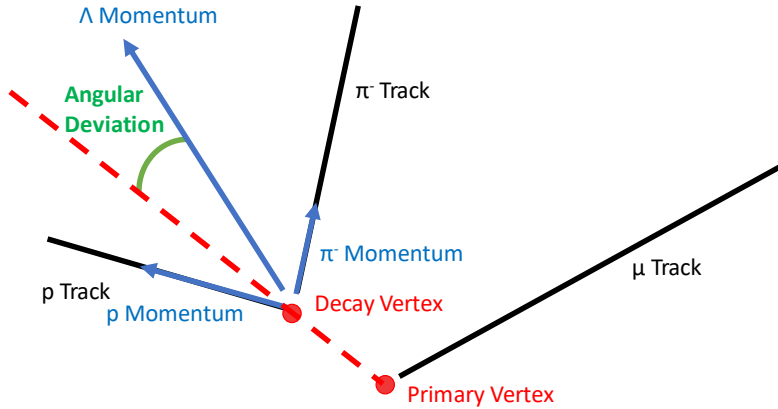


Figure 5: Calculation of the angular deviation variable.

## B Partial Phase Space Definition

As the selection can only identify  $\Lambda$ 's that decay into a proton and  $\pi^-$  with momenta above detection thresholds, the cross section must be corrected to only include this portion of the phase space. Our restricted phase space cross section  $\sigma_*$  is related to the total cross section for quasi-elastic  $\Lambda$  production by:

$$\sigma_* = F\sigma, \quad (5)$$

$$F = \frac{1}{\sigma} \int_0^\infty f(p_\Lambda) \frac{d\sigma}{dp_\Lambda} dp_\Lambda. \quad (6)$$

$f(p_\Lambda)$  is the fraction of  $\Lambda$ 's decaying via  $\Lambda \rightarrow p + \pi^-$  that will be above the detection thresholds. This function is shown in Fig. 6, and may be calculated with:

$$f(p_\Lambda) = \begin{cases} 0 & \text{if } A > B \\ \frac{B-A}{2} & \text{Otherwise} \end{cases}, \quad (7)$$

$$A = \max \left( \frac{\sqrt{M_p^2 + |p_p^{\text{thresh}}|^2} - \gamma E_p}{\beta \gamma p}, -1 \right), \quad (8)$$

$$B = \min \left( \frac{-\sqrt{M_\pi^2 + |p_\pi^{\text{thresh}}|^2} + \gamma E_\pi}{\beta \gamma p}, 1 \right), \quad (9)$$

$$E_p = \sqrt{M_p^2 + p^2}, \quad (10)$$

$$E_\pi = \sqrt{M_\pi^2 + p^2}, \quad (11)$$

where  $M_p$  and  $M_\pi$  are the rest masses of the proton and  $\pi^-$  respectively,  $p_p^{\text{thresh}} = 0.3$  GeV,  $p_\pi^{\text{thresh}} = 0.1$  GeV,  $p = 0.101$  GeV,  $\beta$  is the boost factor of the  $\Lambda$  baryon in the detector's frame, and  $\gamma = 1/\sqrt{1 - \beta^2}$ . Natural units are used.

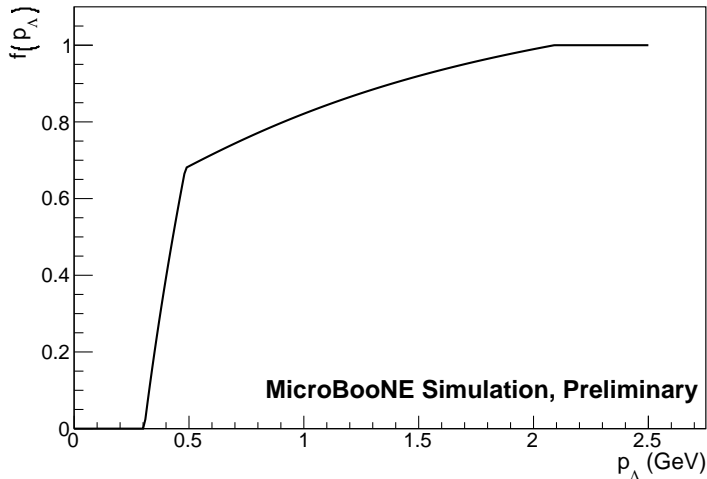


Figure 6: The function  $f(p_\Lambda)$  featured in equations. 2 and 3. The two discontinuities in gradient occur when one, and then both particles produced in the decay is always above the detection threshold.

## C Flux

Fig. 7 displays the fluxes used in Monte Carlo simulations, including the combined neutrino mode (forward horn current, FHC) and anti-neutrino mode (reverse horn current, RHC) flux that corresponds to the data taking period analyzed. The  $\bar{\nu}_\mu$  flux corresponding to the data taking periods analyzed is a weighted average of the FHC and RHC fluxes.

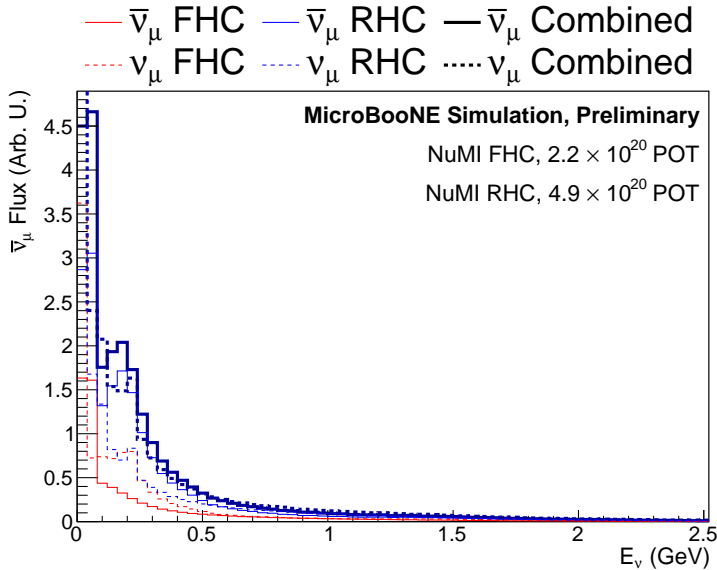


Figure 7: The neutrino and anti-neutrino fluxes corresponding to the data analyzed.

## D Island Finding Algorithm

In order to determine if the  $\Lambda$  candidate in the event forms a true secondary vertex, instead of analyzing the reconstructed tracks, the post-deconvolution wire activity is used, the raw form of which may be seen in Fig. 1 of the letter this material supports, and in Figs. 8a and 9a below. This may be interpreted as a grid, in which a single square has the dimensions of one channel by one time tick, and stores the level of activity recorded on that wire at that time.

The first stage of the algorithm is to scan through every square in this grid and remove any with activity below a pre-defined threshold. Any squares above the threshold are all assigned a single value to indicate they are “occupied”, the output of this stage is shown in Figs. 8b and 9b. The starting positions of the muon, proton, and pion tracks, transformed into channel-tick space, are used as “seeds” of islands, shown in cyan in Figs. 8c and 9c, and any neighboring squares that are occupied are added to their respective islands, and then the squares that neighbor those. This is done recursively until no new squares can be added. During this process, if any two islands meet, they will merge, and this merging is recorded. Fig. 8c shows two separate islands, with the muon island shown in blue, and the merged proton and pion in pink, while in Fig. 9c, all three islands merged. The passing condition is that the proton and pion islands must merge, while the muon remains separate. This is performed using the activity from each of the three wire planes separately, and events that pass this test in at least one plane are selected.

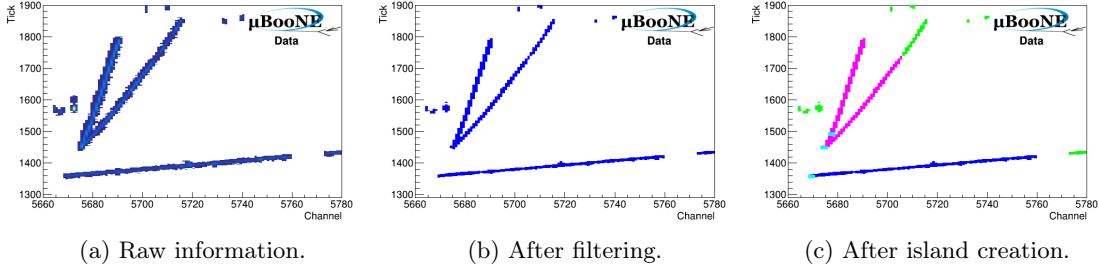


Figure 8: The three stages of the island finding algorithm, shown for the event selected from the data in Fig. 1 of the letter. The blue and pink regions in panel 8c indicate the islands produced by the muon track and  $\Lambda$  candidate respectively. The green regions correspond to wire activity not belonging to any either. The cyan squares show are starting positions of the three tracks when viewed from this wire plane.

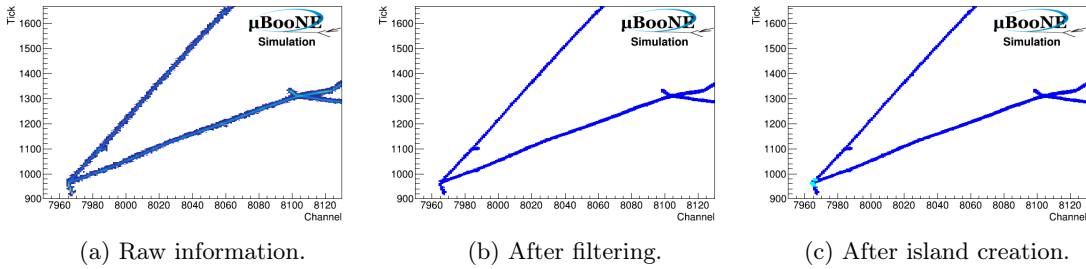


Figure 9: The three stages of the island finding algorithm, shown for a MC simulation event that failed this stage of the selection.

## E Sidebands

To confirm the background Monte Carlo simulation predictions are consistent with data, two sidebands are employed. The first, shown in Figs. 10a and 11a, is created by inverting the cut applied to the invariant mass, and the second, in Figs. 10b and 11b, by inverting the cut on the angular deviation. Data and MC predictions using both the NuMI Beam, and the Booster Neutrino Beam (BNB) are compared. In the case of the NuMI data, the signal region is kept blind. The BNB data is expected to be extremely signal poor due to the low anti-neutrino flux produced by the beam, and the signal region is not kept blind, providing a check on the hyperon induced background. The Monte Carlo simulation predictions for the BNB do not include systematic uncertainties.

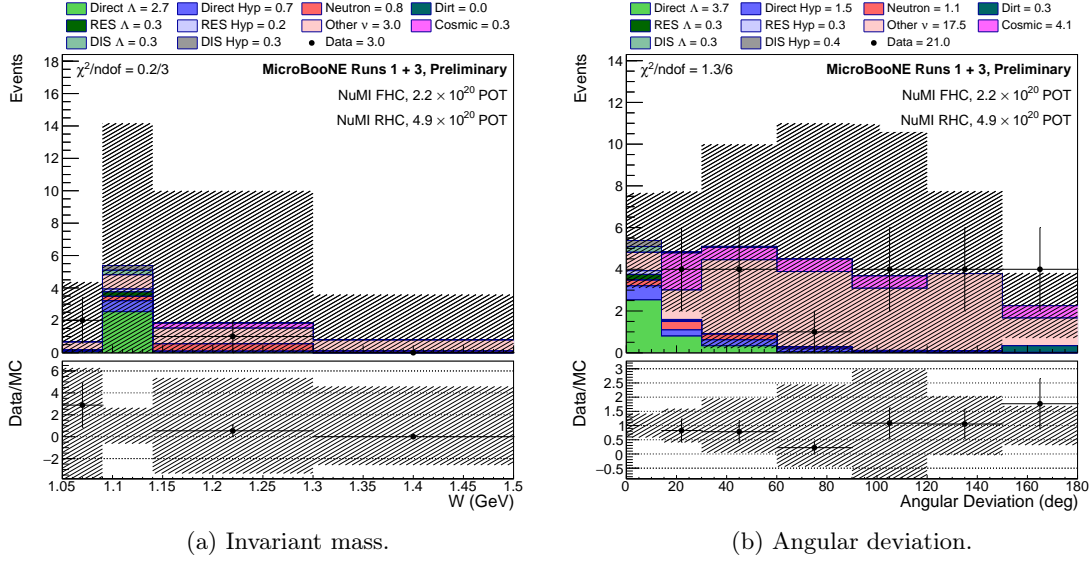


Figure 10: Sideband distributions constructed using NuMI data, the signal bin was kept blind.

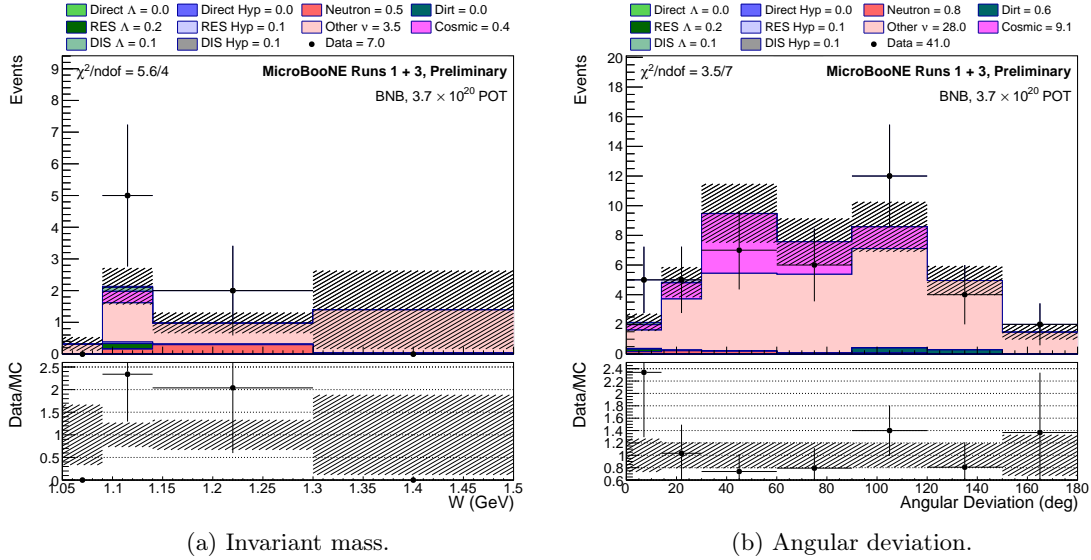


Figure 11: Sideband distributions constructed using BNB data.

## F Constraint Procedure

The visual scan is employed to remove background containing reconstruction problems, for which the MC simulation does not produce enough events to estimate the corresponding uncertainties in the signal region correctly. An alternative approach tested was to perform a constraint procedure using data passing the automated selection, but inverting the cuts applied to the angular deviation and invariant mass. This data is split into two sets: a near sideband, containing events with angular deviations  $< 50^\circ$  and  $1.08 < W < 1.3$  GeV, and a far sideband, containing everything else.

A fit is then performed, varying the size of the bad-reconstruction background (“Other  $\nu$ ” in Fig. 12), producing a new prediction shown in Fig. 12b. To obtain systematic uncertainties, we perform this fit in each systematic universe to obtain data-constrained sets of variations in

the bad reconstruction background, which are then used to calculate the covariance between the flux, background, and efficiency. The extracted cross section is  $1.6_{-1.4}^{+2.0} \times 10^{-40} \text{ cm}^2$ ; the Bayesian posterior distribution is presented in Fig. 13.

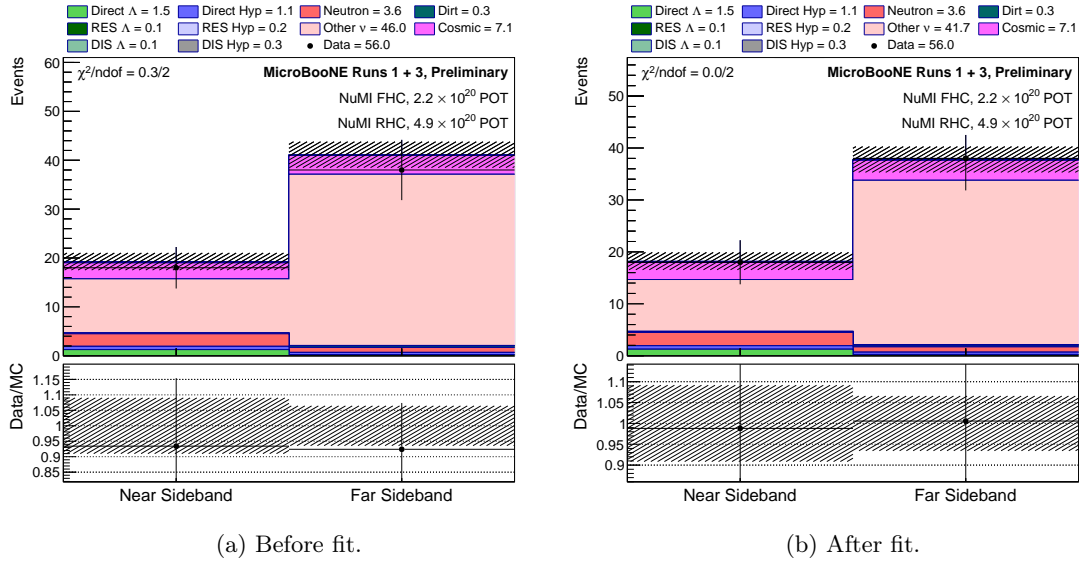


Figure 12: The data from the sideband compared with MC simulation before and after performing the fit.

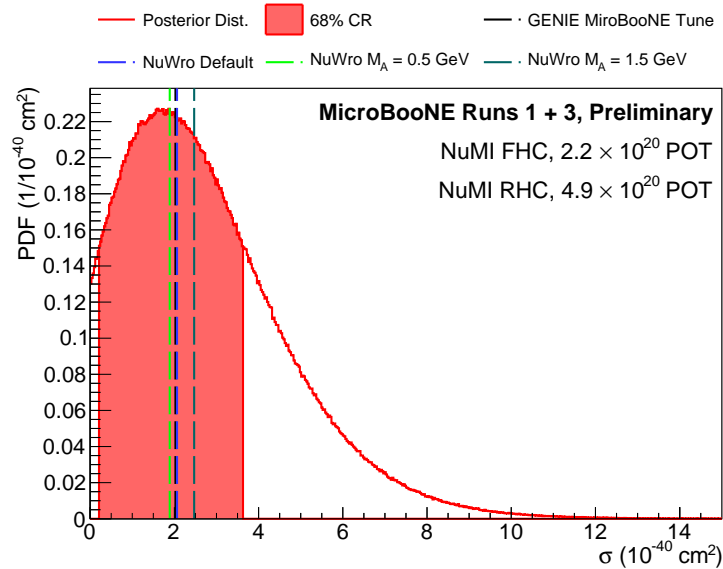
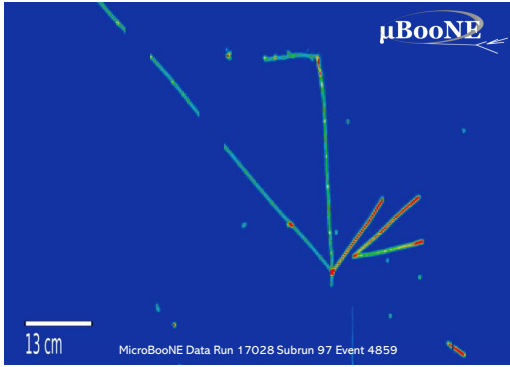


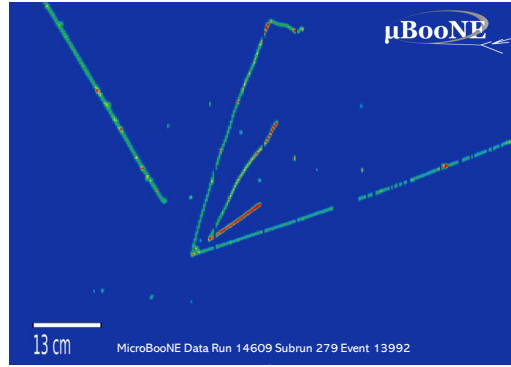
Figure 13: Bayesian posterior probability distribution of the extracted cross section obtained when employing the sideband constraint procedure.

## G Selected Data

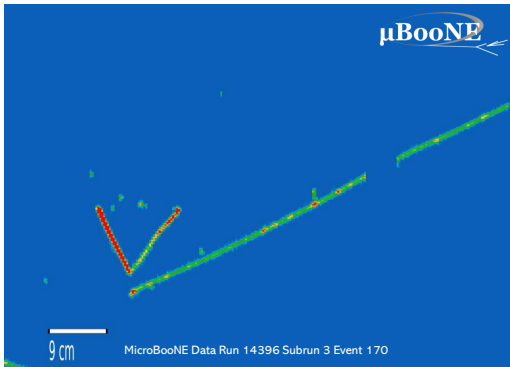
The five  $\Lambda$  production candidates identified in the data by the automated selection are displayed below. The events selected from among these by each of the visual scanners are indicated in Table 2.



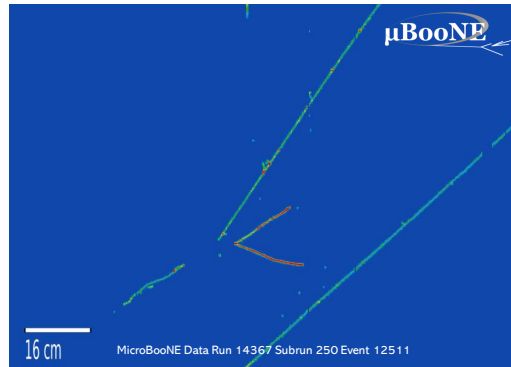
(a) Run 17028 subrun 97 event 4859.



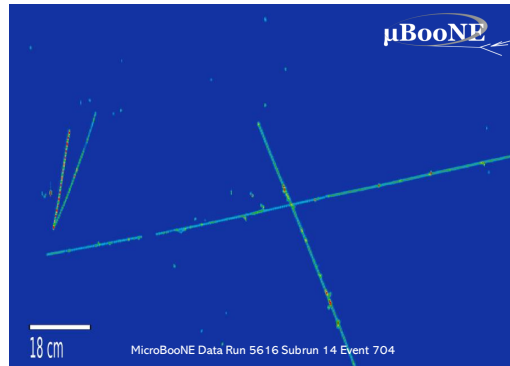
(b) Run 14609 subrun 279 event 13992.



(c) Run 14396 subrun 3 event 170.



(d) Run 14367 subrun 250 event 12511.



(e) Run 5616 subrun 14 event 704.

Figure 14: The  $\Lambda$  candidates identified in the data by the automated selection.

Run	Subrun	Event	Sc. 1	Sc. 2	Sc. 3	Sc. 4	Sc. 5
17028	97	4859			✓		✓
14609	279	13992	✓		✓		
14396	3	170	✓	✓	✓	✓	✓
14367	250	12511	✓	✓	✓	✓	✓
5616	14	704	✓	✓	✓	✓	✓

Table 2: The events selected from the data by each of the five scanners.